Photon-Counting Detector CT for Liver Lesion Detection-Optimal Virtual Monoenergetic Energy for Different Simulated Patient Sizes and Radiation Doses

Racine, Damien ; Mergen, Victor ; Viry, Anaïs ; Frauenfelder, Thomas ; Alkadhi, Hatem ; Vitzthum, Veronika ; Euler, André

DOI: https://doi.org/10.1097/RLI.0000000000001060

OPEN

Photon-Counting Detector CT for Liver Lesion Detection—Optimal Virtual Monoenergetic Energy for Different Simulated Patient Sizes and Radiation Doses

Damien Racine, PhD, Victor Mergen, MD, Anaïs Viry, PhD, Thomas Frauenfelder, MD, Hatem Alkadhi, MD, MPH, Veronika Vitzthum, PhD, and André Euler, MD, MHBA

Objectives: The aim of this study was to evaluate the optimal energy level of virtual monoenergetic images (VMIs) from photon-counting detector computed tomography (CT) for the detection of liver lesions as a function of phantom size and radiation dose.

Materials and Methods: An anthropomorphic abdominal phantom with liver parenchyma and lesions was imaged on a dual-source photon-counting detector CT at 120 kVp. Five hypoattenuating lesions with a lesion-to-background contrast difference of −30 HU and −45 HU and 3 hyperattenuating lesions with +30 HU and +90 HU were used. The lesion diameter was 5–10 mm. Rings of fat-equivalent material were added to emulate medium- or large-sized patients. The medium size was imaged at a volume CT dose index of 5, 2.5, and 1.25 mGy and the large size at 5 and 2.5 mGy, respectively. Each setup was imaged 10 times. For each setup, VMIs from 40 to 80 keV at 5 keV increments were reconstructed with quantum iterative reconstruction at a strength level of 4 (QIR-4). Lesion detectability was measured as area under the receiver operating curve (AUC) using a channelized Hotelling model observer with 10 dense differences of Gaussian channels.

Results: Overall, highest detectability was found at 65 and 70 keV for both hypoattenuating and hyperattenuating lesions in the medium and large phantom independent of radiation dose (AUC range, 0.91–1.0 for the medium and 0.94–0.99 for the large phantom, respectively). The lowest detectability was found at 40 keV irrespective of the radiation dose and phantom size (AUC range, 0.78–0.99). A more pronounced reduction in detectability was apparent at 40–50 keV as compared with 65–75 keV when radiation dose was decreased. At equal radiation dose, detection as a function of VMI energy differed stronger for the large size as compared with the medium-sized phantom (12% vs 6%).

Conclusions: Detectability of hypoattenuating and hyperattenuating liver lesions differed between VMI energies for different phantom sizes and radiation doses. Virtual monoenergetic images at 65 and 70 keV yielded highest detectability independent of phantom size and radiation dose.

Key Words: liver, phantom, photon-counting CT, lesion detectability, radiation dose, image reconstruction, VMI optimization

(*Invest Radiol* 2024;00: 00–00)

Photon-counting detector computed tomography (PCD-CT)'s inherent spectral capabilities enable the reconstruction of virtual monoenergetic images (VMIs), which have become the default reconstruction for diagnostic readings.[1–4] In traditional energy-integrating detector CT (EID-CT), VMIs have demonstrated increased contrast-to-noise ratio (CNR) of iodinated structures, increased lesion conspicuity,[5] and reduced beam-hardening.[6] In addition, former research has indicated that the use of VMI from PCD-CT may enable radiation dose reduction while improving diagnostic performance as compared with EID-CT.[7–10] However, one of the challenges using VMI from EID-CT was that the optimal VMI energy depended on the size of the patient and the diagnostic task.[11–14] Attenuation properties of tissues and noise texture may vary between small and large patients due to photon statistics, including the number of detected photons and the corresponding statistical fluctuations.[15–17] Thus, the VMI energy needs to be adjusted as a function of patient size to optimize lesion detectability.[18–20] Previous studies suggested that smaller patients may require lower energy levels to achieve optimal image quality, whereas larger patients may require higher energy levels to overcome increased attenuation and improve the CNR of iodinated structures.[14,19] Therefore, an understanding of the relationship between patient size and the optimal VMI energy for lesion detection is crucial to provide accurate and reliable diagnoses in different patient populations and clinical scenarios.

The purpose of our experimental study was to determine the optimal VMI energy from PCD-CT for the detection of hypoattenuating and hyperattenuating liver lesions as a function of phantom size and radiation dose.

MATERIALS AND METHODS

Phantom Design

An anthropomorphic abdominal phantom (QSA-453 and QSA-637; QRM, Moehrendorf, Germany) was used. A liver insert, consisting of a uniform background liver parenchyma and several lesions with varying attenuation values, was placed in the phantom. The background attenuation was equal to 90 Hounsfield units (HU) at 120 kVp, as shown in Figure 1. Within the liver parenchyma, there were 5 iodinated hypoattenuating and 3 hyperattenuating spherical lesions or capsular focal lesions with an elliptical shape. Size and lesion-to-background contrast of the hypoattenuating lesions were 5 mm/−30 HU, 10 mm/−30 HU, 5 mm/−45 HU, 5 × 7.5 mm/−30 HU, and 7.5 × 5 mm/−30 HU, respectively. Size and lesion-to-background contrast of the hyperattenuating lesions were 5 mm/+90 HU, 10 mm/+30 HU, and 5 × 7.5 mm/+30 HU, respectively.

Received for publication October 18, 2023; and accepted for publication, after revision, November 22, 2023.

From the Institute of Radiation Physics, University Hospital Lausanne (CHUV), University of Lausanne, Lausanne, Switzerland (D.R., A.V., V.V.); Diagnostic and Interventional Radiology, University Hospital Zurich, University of Zurich, Zurich, Switzerland (V.M., T.F., H.A., A.E.); and Department of Radiology, Kantonsspital Baden, Baden, Switzerland (A.E.).

Conflicts of interest and sources of funding: The Institute of Diagnostic and Interventional Radiology of the University Hospital Zurich received institutional grants from Bayer Healthcare AG, Canon, Guerbet, and Siemens Healthcare GmbH unrelated to this study. In addition, A.E. and H.A. are part of the speaker's bureau of Siemens. Other authors declare that the research was conducted in the absence of any commercial or financial relationships that could be construed as a potential conflict of interest.

Correspondence to: André Euler, MD, MHBA, Department of Radiology, Kantonsspital Baden, Im Ergel 1, 5404 Baden, Switzerland. E-mail: andre.euler@ksb.ch.

ISSN: 0020-9996/24/0000–0000
DOI: 10.1097/RLI.0000000000001060

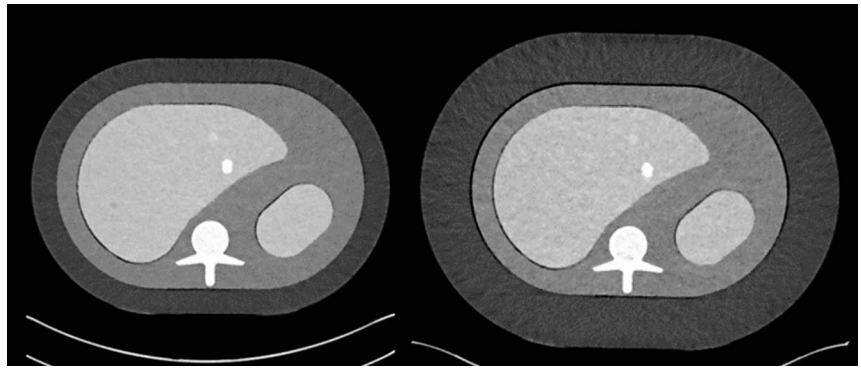

FIGURE 1. Phantom setup. Representative axial CT images of the medium (left) and large (right) anthropomorphic abdominal phantoms.

To vary the morphology of the phantom and simulate normal weight and overweight patients, rings of fat-equivalent material (M = 250 × 350 mm; L = 300 × 400 mm in thickness) were added (see Fig. 1).

Scan Protocol and Reconstruction Settings

The phantom was imaged using the spectral single-source mode at 120 kVp on a first-generation clinical dual-source PCD-CT (NAEOTOM Alpha, Siemens, Syngo CT VA50). Radiation doses were varied by adjusting the image quality index to achieve a volume CT dose index of 5, 2.5, and 1.25 mGy, respectively, for the medium-sized phantom, and 5 and 2.5 mGy for the large-sized phantom. Scanning was repeated 10 times for each setup to obtain sufficient statistics. Estimation of detectability bias and uncertainty decreased with increasing numbers of images.[21]

Each dataset was reconstructed as VMI from 40 to 80 keV at 5 keV increments applying the quantum iterative reconstruction algorithm (QIR, VA50, Siemens) at a strength level of 4 (QIR-4) with kernel Br36. A strength level of 4 was chosen based on the results of a prior study, which demonstrated superior lesion detectability at this strength level as compared with lower strength levels.[7] Scan acquisition and image reconstruction parameters are summarized in Table 1.

Assessment of Lesion Detectability

Lesion detectability was evaluated using a channelized Hotelling model observer with 10 dense differences of Gaussian channels following the methodology proposed by Racine et al.[22] This mathematical observer mimics human observer responses for the detection of low contrast image objects.[23–25] The observer was applied to sets of signal-absent images (150 images) and signal-present images (50 images for hypoattenuating and 30 images for hyperattenuating lesions) to calculate the average area under the receiver operating curve (AUC), which served as the figure of merit for lesion detectability. Area under the receiver operating curve was assessed for hypoattenuating and hyperattenuating lesions. Internal noise was added to the images to account for the variability in human perceptual processes. Internal noise is a proportional factor added to the covariance matrix calculated from 150 signal-absent images to emulate human results.[26]

Statistical Analysis

The performance of the channelized Hotelling model observer was assessed using the 95% confidence interval estimators, which were calculated using the method developed by Wunderlich et al.[27] For lesion detectability, the confidence intervals were used to determine statistical significance between the AUC values for different VMI energies and phantom sizes. To determine if the difference between the maximum value and other values is statistically significant, the 95% confidence interval for the difference was calculated. If the 95% confidence interval did not include zero, we concluded that the difference was significantly different from zero. If the 95% confidence interval included zero, we concluded that the difference was not significantly different from zero.

TABLE 1. Scan Acquisition and Image Reconstruction Parameters

	Medium Phantom	Large Phantom
Radiation dose ($CTDI_{vol}$ in mGy)	5/2.5/1.25	5/2.5
Data acquisition		
Tube potential (kVp)	120	120
Quality reference mAs	104/52/26	104/52
Gantry revolution time (s)	0.5	0.5
Detector collimation (mm)	144 × 0.4	144 × 0.4
Pitch	0.8	0.8
Image reconstruction		
Display field of view (mm)	370 × 370	420 × 420
Section thickness (mm)	3.0	3.0
Section overlap (mm)	1.5	1.5
Kernel	Br36	Br36
Quantum iterative reconstruction (QIR)	Strength level 4	Strength level 4
Reconstruction	40–80 keV at 5 keV increment	40–80 keV at 5 keV increment

$CTDI_{vol}$, volume CT dose index; VMIs, virtual monoenergetic images.

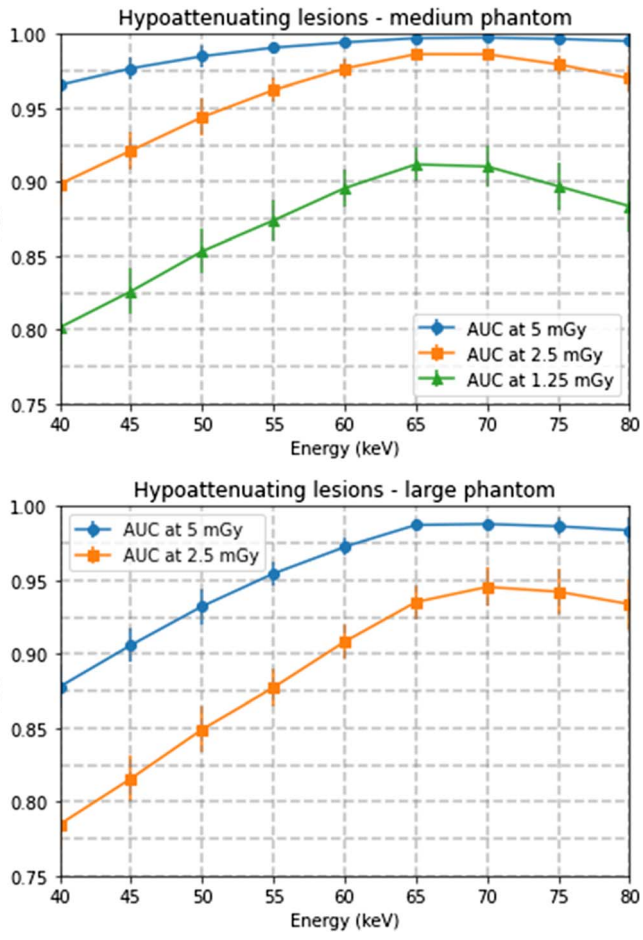

FIGURE 2. Diagnostic accuracy (AUC) for hypoattenuating focal liver lesions as a function of VMI energy at different radiation doses for the medium (top) and large (bottom) size phantom.

RESULTS

Lesion Detectability

Hypoattenuating Lesions

Detectability of hypoattenuating lesions as a function of VMI energy and radiation dose are summarized in Figure 2. Results are reported in Table 2 for the medium-sized phantom and Table 3 for the large-sized phantom, respectively.

Lesion detectability was lowest for VMI at 40 keV for all radiation doses and phantom sizes. For both the medium- and the large-sized phantom, lesion detectability gradually improved with increasing VMI energies, starting at 40 keV before reaching a maximum. For the medium-sized phantom, this maximum was found at 70 keV for 5 mGy, at 65 and 70 keV for 2.5 mGy, and at 65 keV for 1.25 mGy, respectively. For the large-sized phantom, this maximum was found at 65 keV and 70 keV for 5 mGy and at 70 keV for 2.5 mGy. After reaching this maximum, lesion detectability decreased at energies higher than 70 keV. Regardless of the phantom size, AUC was higher at higher radiation dose.

Radiation dose reduction influenced detectability stronger at 40 keV as compared with 65 and 70 keV (loss in lesion detectability between highest and lowest radiation doses of −17% for 40 keV and −8% for 65–70 keV in the medium phantom and of −10% vs −4% in the large phantom). In addition, choosing the optimal VMI energy compared with the worst VMI energy improved detection stronger in the large phantom (ie, +17% vs +8.9% at 2.5 mGy for the large-sized and the medium-sized phantom, respectively). The lesion detectability at the lowest radiation dose using the optimal VMI energy was higher as compared with 40 keV at doubled radiation dose (0.912 ± 0.011 for 65 keV at 1.25 mGy vs 0.898 ± 0.015 for 40 keV at 2.5 mGy in the medium phantom; 0.945 ± 0.013 for 70 keV at 2.5 mGy vs 0.877 ± 0.014 for 40 keV at 5 mGy in the large phantom).

Figure 3 exhibits the corresponding images of the lesions.

Hyperattenuating Lesions

Detectability of hyperattenuating lesions as a function of VMI energy and radiation dose are summarized in Figure 4. Results are reported in Table 4 for the medium-sized phantom and Table 5 for the large-sized phantom, respectively. Figure 5 exhibits the corresponding images of the lesions.

Lesion detectability was lowest at 40 keV for all radiation doses and phantom sizes. Lesion detectability gradually improved with increasing VMI energies, reaching a maximum at 70 keV for 5 mGy

TABLE 2. Detectability of Hypoattenuating Lesions for the Medium Size

	AUC at 5 mGy	AUC at 2.5 mGy	AUC at 1.25 mGy
40 keV	0.97 ± 0.01* (−3.2%)	0.90 ± 0.02* (−8.9%)	0.80 ± 0.02* (−12.1%)
45 keV	0.98 ± 0.01* (−2.1%)	0.92 ± 0.01* (−6.6%)	0.83 ± 0.02* (−9.4%)
50 keV	0.99 ± 0.01 (−1.3%)	0.94 ± 0.01* (−4.3%)	0.86 ± 0.02* (−6.4%)
55 keV	0.99 ± 0.00 (−0.7%)	0.96 ± 0.01* (−2.4%)	0.88 ± 0.01* (−4.2%)
60 keV	0.99 ± 0.00 (−0.3%)	0.98 ± 0.01 (−1.0%)	0.90 ± 0.01 (−1.8%)
65 keV	1.0 ± 0.00 (−0.1%)	0.99 ± 0.00 (N/A)	0.91 ± 0.01 (N/A)
70 keV	1.0 ± 0.00 (N/A)	0.99 ± 0.00 (−0.1%)	0.91 ± 0.01 (−0.2%)
75 keV	1.0 ± 0.00 (−0.2%)	0.98 ± 0.01 (−0.7%)	0.90 ± 0.02 (−1.6%)
80 keV	1.0 ± 0.00 (−0.2%)	0.97 ± 0.01 (−1.7%)	0.88 ± 0.02 (−3.1%)

Data are mean of AUC (rounded to 2 decimals) ± 95% confidence intervals for different VMI energies at 5, 2.5, and 1.25 mGy. Percentage differences compared with the optimal VMI are indicated in brackets. Note that the detection was highest at 65–70 keV, and the minimum was obtained at 40 keV.

*Statistical significance ($P < 0.05$) as compared with the optimal VMI energy at the same radiation dose.

AUC, area under the receiver operating curve; N/A, not applicable.

TABLE 3. Detectability of Hypoattenuating Lesions for the Large Size

	AUC at 5 mGy	AUC at 2.5 mGy
40 keV	0.88 ± 0.01* (−11.1%)	0.78 ± 0.02* (−17.0%)
45 keV	0.91 ± 0.01* (−8.3%)	0.82 ± 0.02* (−13.7%)
50 keV	0.93 ± 0.01* (−5.6%)	0.85 ± 0.02* (−10.2%)
55 keV	0.95 ± 0.01* (−3.4%)	0.88 ± 0.01* (−7.2%)
60 keV	0.97 ± 0.01* (−1.6%)	0.91 ± 0.01* (−3.9%)
65 keV	0.99 ± 0.00 (−0.1%)	0.94 ± 0.01 (−1.1%)
70 keV	0.99 ± 0.00 (N/A)	0.95 ± 0.01 (N/A)
75 keV	0.99 ± 0.01 (−0.2%)	0.94 ± 0.02 (−0.3%)
80 keV	0.98 ± 0.01 (−0.4%)	0.93 ± 0.02 (−1.2%)

Data are mean of AUC (rounded to 2 decimals) ± 95% confidence intervals for different VMI energies at 5 and 2.5 mGy. Percentage differences compared with the optimal VMI are indicated in brackets. Note that the detection was overall highest at 70 keV for both radiation doses.

*Statistical significance ($P < 0.05$) as compared with the optimal VMI energy at the same radiation dose.

AUC, area under the receiver operating curve; N/A, not applicable.

and 2.5 mGy, and at 65 keV for 1.25 mGy for the medium-sized phantom. For the large phantom, the highest detectability was found at 65 keV for 5 mGy and at 70 keV for 2.5 mGy. After reaching a maximum, lesion detectability slightly decreased at higher VMI energies.

Radiation dose reduction influenced detectability stronger at 40 keV as compared with 65 and 70 keV (loss in lesion detectability between highest and lowest radiation doses of −13% for 40 keV and −5% for 70 keV in the medium phantom and of −12% vs −3% in the large phantom). Again, choosing the optimal VMI energy compared with the worst VMI energy improved detection stronger in the large phantom (ie, +13.6% vs +3.9% at 2.5 mGy for the large-sized and the medium-sized phantom, respectively). The lesion detectability at the lowest radiation dose using the optimal VMI energy was higher as compared with 40 keV at doubled radiation dose.

DISCUSSION

Former research has indicated that VMIs from PCD-CT potentially enable higher lesion image quality (ie, lesion detectability or conspicuity) as compared with polychromatic images from conventional EID-CT.[7,8,28] However, the optimal VMI energy to detect liver lesions as a function of patient size and radiation dose has not yet been determined for PCD-CT. This study systematically assessed the optimal VMI energy to detect hypoattenuating and hyperattenuating liver lesions with respect to different patient sizes and radiation doses using a PCD-CT and a model observer. Traditional human observer studies are very time-consuming, and reader performance is variable compromising the reproducibility of the results. Model observers have been developed to overcome these limitations, enabling objective assessment of CT technology under controlled conditions. Our results indicate that the highest detectability for both hypoattenuating and hyperattenuating lesions was achieved using VMI at 65 or 70 keV. In addition, the impact of changes in radiation dose was minimized by using the optimal VMI energy. These results differed from previous studies that investigated the optimal VMI energy for liver imaging using

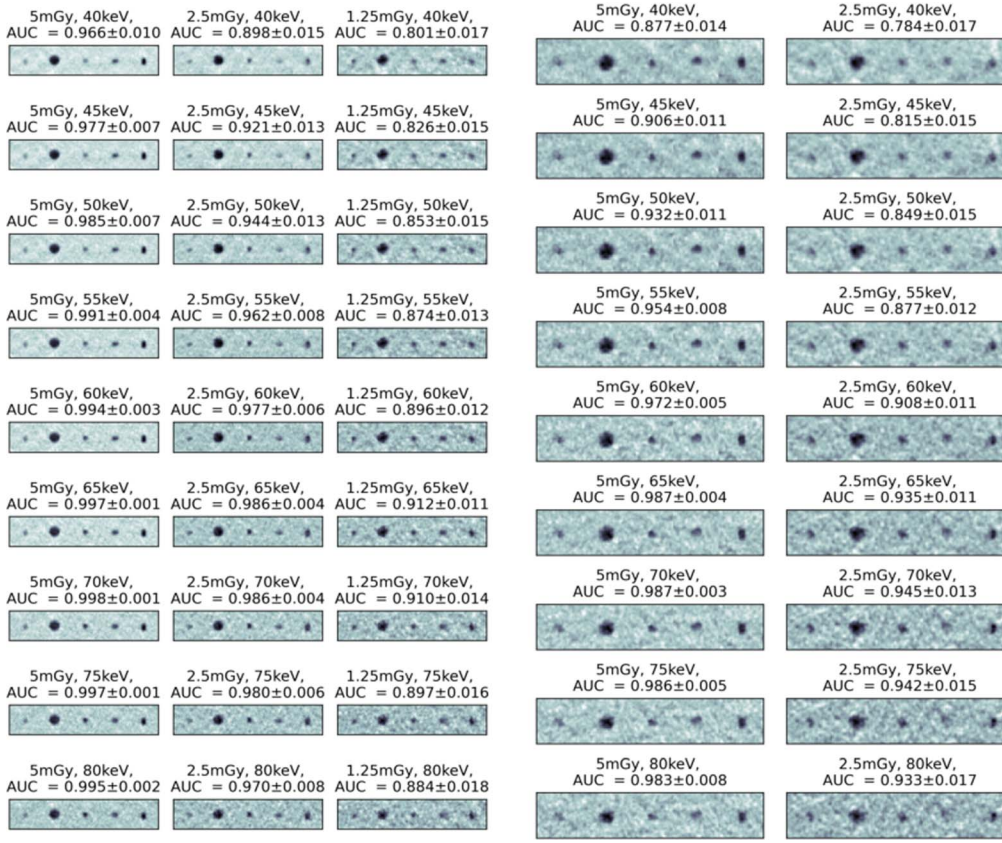

FIGURE 3. Regions of interest of each hypoattenuating focal liver lesion of the medium phantom (left) and large phantom (right) as a function of radiation dose and VMI energy. AUC values are listed. Images were obtained by averaging 10 repeated scans. Lesions from left to right: 5 mm/−30 HU, 10 mm/−30 HU, 5 mm/−45 HU, 5 × 7.5 mm/−30 HU, and 7.5 × 5 mm/−30 HU.

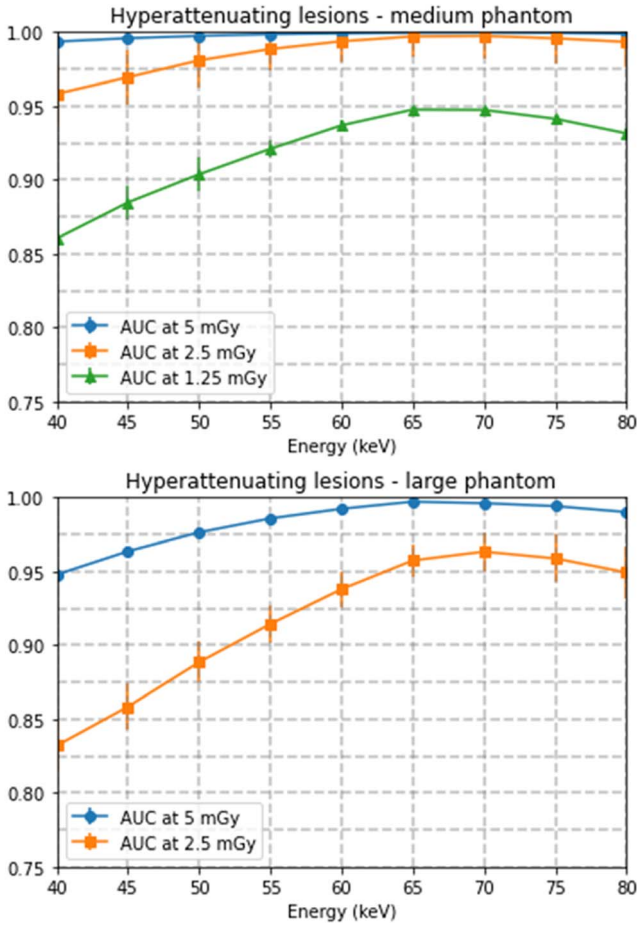

FIGURE 4. Diagnostic accuracy for hyperattenuating focal liver lesions. AUC for hyperattenuating focal liver lesions as a function of VMI energy at different radiation doses for medium phantom (top) and large phantom (bottom).

EID-CT and PCD-CT. Higashigaito et al[28] found that VMI at 50 keV provided the best trade-off between objective and subjective image quality at maintained liver lesion conspicuity. In addition, Graafen et al[29] found that liver lesion conspicuity was high on VMI at 65 keV or lower energies but worsened when using VMI at 70 keV or higher energies. Although both studies focused on image quality and lesion conspicuity, lesion detectability was not assessed. Lesion detectability was significantly lower for the large phantom as compared with the medium phantom in our study. One possible reason for this could be higher image noise, which is observed in larger patients as demonstrated by Decker et al[30] who investigated low-dose CT of the abdomen with PCD-CT. Comparing PCD-CT to EID-CT, Euler et al[12] and Bette et al[31] observed a higher gain in CNR and a higher reduction in image noise in obese patients than in normal weight patients when using optimal VMI energies. This gain was also reflected by the larger improvement in detection when choosing the optimal VMI energy in the large phantom as compared with the medium phantom in our study. We found higher lesion detectability for hyperattenuating lesions than for hypoattenuating lesions. This may be mainly due to a higher average contrast difference of 45 HU for hyperattenuating lesions as compared with an average contrast difference of 35 HU for hypoattenuating lesions in our phantom.

Our findings suggest that the optimization of the VMI energy can be used for radiation dose optimization. As an example, in the large

TABLE 5. Detectability of Hyperattenuating Lesions for the Large Size

	AUC at 5 mGy	AUC at 2.5 mGy
40 keV	0.95 ± 0.01* (−5.0%)	0.83 ± 0.02* (−13.6%)
45 keV	0.96 ± 0.01* (−3.4%)	0.86 ± 0.02* (−10.9%)
50 keV	0.98 ± 0.01* (−2.1%)	0.89 ± 0.01* (−7.8%)
55 keV	0.99 ± 0.00* (−1.1%)	0.91 ± 0.01* (−5.1%)
60 keV	0.99 ± 0.00 (−0.5%)	0.94 ± 0.01 (−2.6%)
65 keV	1.0 ± 0.00 (N/A)	0.96 ± 0.01 (−0.6%)
70 keV	1.0 ± 0.00 (−0.1%)	0.96 ± 0.01 (N/A)
75 keV	1.0 ± 0.00 (−0.3%)	0.96 ± 0.02 (−0.5%)
80 keV	1.0 ± 0.00 (−0.7%)	0.95 ± 0.02 (−1.6%)

Data are mean of AUC (rounded to 2 decimals) ± 95% confidence intervals for different VMI energies at 5 and 2.5 mGy. Percentage differences compared with the optimal VMI are indicated in brackets. Note that the detection was highest at 65–70 keV.

*Statistical significance ($P < 0.05$) as compared with the optimal VMI energy at the same radiation dose.

AUC, area under the receiver operating curve; N/A, not applicable.

TABLE 4. Detectability of Hyperattenuating Lesions for the Medium Size

	AUC at 5 mGy	AUC at 2.5 mGy	AUC at 1.25 mGy
40 keV	0.99 ± 0.00 (−0.6%)	0.96 ± 0.01* (−3.9%)	0.86 ± 0.02* (−9.2%)
45 keV	1.00 ± 0.00 (−0.4%)	0.97 ± 0.01* (−2.8%)	0.88 ± 0.02* (−6.6%)
50 keV	1.00 ± 0.00 (−0.2%)	0.98 ± 0.01 (−1.7%)	0.90 ± 0.02 (−4.6%)
55 keV	1.00 ± 0.00 (−0.1%)	0.98 ± 0.01 (−0.9%)	0.92 ± 0.01 (−2.8%)
60 keV	1.00 ± 0.00 (−0.1%)	0.99 ± 0.00 (−0.4%)	0.94 ± 0.01 (−1.1%)
65 keV	1.00 ± 0.00 (−0.1%)	1.00 ± 0.00 (−0.1%)	0.95 ± 0.01 (N/A)
70 keV	1.00 ± 0.00 (N/A)	1.00 ± 0.00 (N/A)	0.95 ± 0.02 (−0.1%)
75 keV	1.00 ± 0.00 (−0.1%)	1.00 ± 0.00 (−0.2%)	0.94 ± 0.02 (−0.7%)
80 keV	1.00 ± 0.00 (−0.1%)	0.99 ± 0.00 (−0.4%)	0.93 ± 0.02 (−1.7%)

Data are mean of AUC (rounded to 2 decimals) ± 95% confidence intervals for different VMI energies at 5, 2.5, and 1.25 mGy. Percentage differences compared with the optimal VMI are indicated in brackets. Note that the detection was highest at 65 and 70 keV independent of dose.

*Statistical significance ($P < 0.05$) as compared with the optimal VMI energy at the same radiation dose.

AUC, area under the receiver operating curve; N/A, not applicable.

FIGURE 5. Regions of interest of each hyperattenuating focal liver lesion of the medium (left) and large (right) phantom as a function of radiation dose and VMI energy. AUC values are listed. Images were obtained by averaging 10 repeated scans. Lesions from left to right: 5 × 7.5 mm/−30 HU, 7.5 × 5 mm/−30 HU, 5 mm/−45 HU, 5 mm/−30 HU, and 10 mm/−30 HU.

phantom, the detectability was similar between 50 keV at 5 mGy and 65 keV at 2.5 mGy for hypoattenuating lesions and between 40 keV at 5 mGy and 65 keV at 2.5 mGy for hyperattenuating lesions. This offers radiation dose reduction if an optimal VMI energy is chosen dependent on the clinical task.

The following limitations merit consideration. First, the study was conducted using an anthropomorphic abdominal phantom that may not accurately represent the complexity of the human body. The results found here need to be validated in patients with human readers (ie, radiologists) assessing detectability, detection conspicuity, and subjective image quality. Second, scans were solely reconstructed using routine parameters. The impact of different kernels and quantum iterative reconstruction strength levels on the detectability was not investigated. Based on the findings of Graafen et al[32] who demonstrated that soft reconstruction kernels yield the best overall quality for the evaluation of hepatocellular carcinoma in PCD-CT, a soft kernel (Br36) was used. Similarly, quantum iterative reconstruction was applied with a strength level of 4 as this strength level is supposed to provide the best image quality as suggested by previous studies.[7,33] Third, scans were acquired with a single tube potential. Booij et al[34] indicated that the tube potential may have an impact on CNR. In the future, it will be interesting to evaluate the impact of the tube potential combined with various VMI energies on lesion detectability. Finally, this evaluation was limited to the detectability of focal liver lesions. Future studies will be needed to find the optimal VMI energy for other abdominal pathologies and quantification tasks.[35]

In conclusion, detectability of liver lesions depended on the radiation dose and phantom size and was considerably improved by selecting the optimal VMI energy. Based on our findings, we suggest VMI at 65 or 70 keV as the optimal VMI energy to detect hypoattenuating or hyperattenuating liver lesions. These findings could serve as a basis to optimize liver imaging protocols of PCD-CT in future clinical trials.

REFERENCES

1. Wildberger JE, Alkadhi H. New horizons in vascular imaging with photon-counting detector CT. *Invest Radiol*. 2023;58:499–504.
2. Si-Mohamed SA, Boccalini S, Villien M, et al. First experience with a whole-body spectral photon-counting CT clinical prototype. *Invest Radiol*. 2023;58:459–471.
3. Remy-Jardin M, Hutt A, Flohr T, et al. Ultra-high-resolution photon-counting CT imaging of the chest: a new era for morphology and function. *Invest Radiol*. 2023; 58:482–487.
4. McCollough CH, Rajendran K, Leng S. Standardization and quantitative imaging with photon-counting detector CT. *Invest Radiol*. 2023;58:451–458.
5. Marin D, Boll DT, Mileto A, et al. State of the art: dual-energy CT of the abdomen. *Radiology*. 2014;271:327–342.
6. Lin XZ, Miao F, Li JY, et al. High-definition CT gemstone spectral imaging of the brain: initial results of selecting optimal monochromatic image for beam-hardening artifacts and image noise reduction. *J Comput Assist Tomogr*. 2011;35:294–297.
7. Racine D, Mergen V, Viry A, et al. Photon-counting detector CT with quantum iterative reconstruction: impact on liver lesion detection and radiation dose reduction. *Invest Radiol*. 2023;58:245–252.
8. Rajagopal JR, Farhadi F, Solomon J, et al. Comparison of low dose performance of photon-counting and energy integrating CT. *Acad Radiol*. 2021;28:1754–1760.

9. Dillinger D, Overhoff D, Booz C, et al. Impact of CT photon-counting virtual monoenergetic imaging on visualization of abdominal arterial vessels. *Diagnostics (Basel)*. 2023;13:938.
10. Sartoretti T, McDermott M, Mergen V, et al. Photon-counting detector coronary CT angiography: impact of virtual monoenergetic imaging and iterative reconstruction on image quality. *Br J Radiol*. 2023;96:20220466.
11. Michalak G, Grimes J, Fletcher J, et al. Selection of optimal tube potential settings for dual-energy CT virtual mono-energetic imaging of iodine in the abdomen. *Abdom Radiol*. 2017;42:2289–2296.
12. Euler A, Higashigaito K, Mergen V, et al. High-pitch photon-counting detector computed tomography angiography of the aorta: intraindividual comparison to energy-integrating detector computed tomography at equal radiation dose. *Invest Radiol*. 2022;57:115–121.
13. Nagayama Y, Iyama A, Oda S, et al. Dual-layer dual-energy computed tomography for the assessment of hypovascular hepatic metastases: impact of closing k-edge on image quality and lesion detectability. *Eur Radiol*. 2019;29:2837–2847.
14. Yu L, Christner JA, Leng S, et al. Virtual monochromatic imaging in dual-source dual-energy CT: radiation dose and image quality. *Med Phys*. 2011;38:6371–6379.
15. Greffier J, Larbi A, Frandon J, et al. Comparison of noise-magnitude and noise-texture across two generations of iterative reconstruction algorithms from three manufacturers. *Diagn Interv Imaging*. 2019;100:401–410.
16. Andersen HK, Völgyes D, Martinsen ACT. Image quality with iterative reconstruction techniques in CT of the lungs—a phantom study. *Eur J Radiol Open*. 2018;5:35–40.
17. Solomon J, Wilson J, Samei E. Characteristic image quality of a third generation dual-source MDCT scanner: noise, resolution, and detectability. *Med Phys*. 2015;42:4941–4953.
18. Cester D, Eberhard M, Alkadhi H, et al. Virtual monoenergetic images from dual-energy CT: systematic assessment of task-based image quality performance. *Quant Imaging Med Surg*. 2022;12:726–741.
19. Mileto A, Nelson RC, Samei E, et al. Dual-energy MDCT in hypervascular liver tumors: effect of body size on selection of the optimal monochromatic energy level. *AJR Am J Roentgenol*. 2014;203:1257–1264.
20. Husarik DB, Gordic S, Desbiolles L, et al. Advanced virtual monoenergetic computed tomography of hyperattenuating and hypoattenuating liver lesions: ex-vivo and patient experience in various body sizes. *Invest Radiol*. 2015;50:695–702.
21. Ba A, Abbey CK, Baek J, et al. Inter-laboratory comparison of channelized Hotelling observer computation. *Med Phys*. 2018;45:3019–3030.
22. Racine D, Ba AH, Ott JG, et al. Objective assessment of low contrast detectability in computed tomography with channelized Hotelling observer. *Phys Med*. 2016;32:76–83.
23. Zhang Y, Leng S, Yu L, et al. Correlation between human and model observer performance for discrimination task in CT. *Phys Med Biol*. 2014;59:3389–3404.
24. Racine D, Ott JG, Ba A, et al. Objective task-based assessment of low-contrast detectability in iterative reconstruction. *Radiat Prot Dosimetry*. 2016;169(1–4):73–77.
25. Solomon J, Samei E. What observer models best reflect low-contrast detectability in CT? In: *Medical Imaging 2015: Image perception, observer performance, and technology Assessment*. 2015;9416. SPIE:102–109. Available at: https://www.spiedigitallibrary.org/conference-proceedings-of-spie/9416/94160I/What-observer-models-best-reflect-low-contrast-detectability-in-CT/10.1117/12.2081655.full. Accessed October 5, 2023.
26. Brankov JG. Evaluation of the channelized Hotelling observer with an internal-noise model in a train-test paradigm for cardiac SPECT defect detection. *Phys Med Biol*. 2013;58:7159–7182.
27. Wunderlich A, Noo F, Gallas BD, et al. Exact confidence intervals for channelized Hotelling observer performance in image quality studies. *IEEE Trans Med Imaging*. 2015;34:453–464.
28. Higashigaito K, Euler A, Eberhard M, et al. Contrast-enhanced abdominal CT with clinical photon-counting detector CT: assessment of image quality and comparison with energy-integrating detector CT. *Acad Radiol*. 2022;29:689–697.
29. Graafen D, Müller L, Halfmann M, et al. Photon-counting detector CT improves quality of arterial phase abdominal scans: a head-to-head comparison with energy-integrating CT. *Eur J Radiol*. 2022;156:110514.
30. Decker JA, Bette S, Lubina N, et al. Low-dose CT of the abdomen: initial experience on a novel photon-counting detector CT and comparison with energy-integrating detector CT. *Eur J Radiol*. 2022;148:110181.
31. Bette S, Decker JA, Braun FM, et al. Optimal conspicuity of liver metastases in virtual monochromatic imaging reconstructions on a novel photon-counting detector CT-effect of keV settings and BMI. *Diagn. Basel Switz*. 2022;12:1231.
32. Graafen D, Müller L, Halfmann MC, et al. Soft reconstruction kernels improve HCC imaging on a photon-counting detector CT. *Acad. Radiol*. 2023;30(Suppl 1):S143–S154.
33. Sartoretti T, Landsmann A, Nakhostin D, et al. Quantum iterative reconstruction for abdominal photon-counting detector CT improves image quality. *Radiology*. 2022;303:339–348.
34. Booij R, van der Werf NR, Dijkshoorn ML, et al. Assessment of iodine contrast-to-noise ratio in virtual monoenergetic images reconstructed from dual-source energy-integrating CT and photon-counting CT data. *Diagnostics (Basel)*. 2022;12:1467.
35. Vrbaski S, Bache S, Rajagopal J, et al. Quantitative performance of photon-counting CT at low dose: virtual monochromatic imaging and iodine quantification. *Med Phys*. 2023;50:5421–5433.